RESEARCH ARTICLE

NANO · MICRO small
www.small-journal.com

Deciphering the Impact of Current, Composition, and Potential on the Lithiation Behavior of Si-Rich Silicon-Graphite Anodes

Philipp Schweigart, Weicheng Hua, Pedro Alonso Sánchez, Camilla Lian, Inger-Emma Nylund, David Wragg, Samson Yuxiu Lai, Federico Cova, Ann Mari Svensson,* and Maria Valeria Blanco**

Adding silicon (Si) to graphite (Gr) anodes is an effective approach for boosting the energy density of lithium-ion batteries, but it also triggers mechanical instability due to Si volume changes upon (de)lithiation reactions. In this work, component-specific (de)lithiation dynamics on Si-rich (30 and 70 wt.% Si) SiGr anodes at various charge/discharge C-rates are unveiled and compared to a graphite-only electrode (100Gr) via operando synchrotron X-ray diffraction coupled with differential capacity plots analysis. Results show preferential lithiation of amorphous Si above ≈200 mV and competing lithiation of Gr, amorphous Si, and crystalline Si below ≈200 mV. Discharge proceeds via sequential delithiation of Gr and amorphous lithium silicide. Si shifts the interconversion potentials of graphite intercalation compounds, lowering the Gr state of charge compared to 100Gr. In the 30% Si electrode, crystalline Si amorphization at potentials <110 mV is found to be kinetically hindered at C-rates higher than C/5, which can be key for enhancing the cycling stability of SiGr anodes. The 70% Si electrode exhibits restricted lithium diffusion in Gr, full Si amorphization, and $Li_{15}Si_4$ formation. These findings related to the potential- and current-dependent dynamic changes on SiGr blends are crucial for designing stable high energy density SiGr anodes.

1. Introduction

In light of recent challenges of electrification, continuous and persistent efforts are made to maximize the energy density of electrochemical energy storage devices. As of today, graphite (Gr) is the predominant anode material in lithium-ion batteries due to its long cycle life, high electrical conductivity, low lithiation potential, low cost, and widespread availability.[1] However, its theoretical capacity of 372 mAh g^{-1} represents a major bottleneck for the development of high energy-density batteries. To address this limitation, alternative anode materials have been extensively researched, with silicon (Si) as one of the most viable candidates.[2] Si exhibits low lithiation potential, high theoretical capacity of ca. 3579 mAh g^{-1}, low cost, and abundance. Nevertheless, the (de)alloying mechanism of Si during (de)lithiation induces volume changes of up to 300%,[3] leading to particle cracking and pulverization and extensive electrolyte consumption due to continuous re-formation of the solid electrolyte interphase (SEI), which results in drastic capacity fade.[4–6]

An effective approach for benefiting from Si high storage capacity while mitigating its mechanical instability is through the development of SiGr blends.[7,8] In these composite anodes, Gr serves as a mechanical buffer, alleviating the volumetric expansion of Si particles, while also enhancing the electronic conductivity of the overall anode.[7]

P. Schweigart, W. Hua, C. Lian, I.-E. Nylund, A. M. Svensson, M. V. Blanco
Department of Materials Science and Engineering
Norwegian University of Science and Technology (NTNU)
Sem Sælands Vei 12, Trondheim 7034, Norway
E-mail: philipp.schweigart@ntnu.no; annmari.svensson@ntnu.no; maria.v.blanco@ntnu.no

The ORCID identification number(s) for the author(s) of this article can be found under https://doi.org/10.1002/smll.202406615

DOI: 10.1002/smll.202406615

P. A. Sánchez
Department of Condensed Matter Physics
Faculty of Sciences
Aragón Nanoscience and Materials Institute (CSIC – University of Zaragoza)
C/Pedro Cerbuna 12, Zaragoza 50009, Spain

D. Wragg, S. Y. Lai
Battery Technology Department
Institute for Energy Technology (IFE)
Instituttveien 18, Kjeller 2007, Norway

F. Cova
BL31 FaXToR Beamline
CELLS- ALBA Synchrotron Light Source
Cerdanyola del Vallès, Barcelona 08290, Spain

Since Gr is the active material in conventional anodes, enhancing their energy density by incorporating Si offers a strategic pathway for minimizing development costs and accelerate time to market. Because of this, development of SiGr blended anodes has become a research hotspot in recent years. Nevertheless, while Gr electrodes exhibit a capacity retention exceeding 99.7 % after 100 cycles, the capacity retention drops to 55.5% for SiGr anodes containing 10 wt.% Si, and further decreases to 25.7% in anodes with 30 wt.% Si.[9]

The pronounced capacity fade of SiGr anodes with increasing Si content has been reported in numerous studies[10–12] and is attributed to both Si volume variations during cycling and the increased electrical resistance of the anode.[13] Additionally, the C-rate significantly influences the lithiation/delithiation dynamics of SiGr anodes, as the Gr lithiation reaction would be limited by slow lithium diffusion at high C-rates,[14] increased resistance due to the presence of Si within the electrode,[15] or a combination of the two.

Although Si in SiGr anodes is either amorphous or becomes amorphous after initial lithiation, the ability to monitor structural changes in the Gr component while simultaneously tracking the anode's electrochemical behavior during cycling has positioned operando X-ray diffraction (XRD) as the technique of choice to gain fundamental insights into local charge transfer mechanisms and the processes underlying capacity fade in SiGr electrodes.[16–21] Operando energy dispersive XRD studies performed on SiGr anodes containing 15 wt.% Si, cycled between 0.01 V and 1 V versus Li/Li^+ at C/30, revealed a lithiation sequence in which Li ions first react with Si particles and subsequently intercalate into the Gr host structure, while the delithiation process would occur first in Gr and then in Si.[22] Similarly, studies on SiO_xGr blends containing 2–8% SiO_x, cycled between 0.01 V and 1.5 V at C/5 during lithiation and at C/100 during delithiation, showed that Li ions first react with SiO_x particles and then with Gr, with a delayed lithiation of Gr in the presence of SiO_x.[23] In contrast, the only operando XRD study in SiGr blends with high Si content, comprising 50 wt.% carbon-coated Si, suggested that Li-ions are initially intercalated and deintercalated in Gr during lithiation and delithiation, respectively, for a cell cycled between 0.005 and 3 V at 0.6 mA.[20] It should be noted that a majority of the operando studies are conducted at low rates, and with a low cut-off of <10 mV.[16,17,19–22] For Si anodes, it is well known that the lower cut-off should be limited to 50 mV in order to avoid the formation of the crystalline $Li_{15}Si_4$ phase, which is highly irreversible.[24]

Despite of the commercial interest in increasing Si content in SiGr anodes for fabricating high energy density negative electrodes, there is a poor understanding at the fundamental level of the complex interplay between Si and Gr components for anodes with different Si content. This knowledge is an essential prerequisite for designing mechanically stable high capacity SiGr anodes. On a fundamental level, the exact mechanism of (de)lithiation in composite anodes has yet to be clarified in the following aspects: 1) The sequential order of Gr and Si lithiation as a function of electrode potential and current. 2) The SOC of Gr and Si components upon cycling. 3) The rate capability limitations of Gr in the composite when it is subjected to high specific currents. 4) Adverse side reactions coinciding with Gr lithiation, such as Si amorphization and buildup of the irreversible $Li_{15}Si_4$ phase.

Table 1. Graphite and Silicon particle size distribution and BET area.

Material	D10 [µm]	D50 [µm]	D90 [µm]	BET [$m^2\ g^{-1}$]
KS-6L	1.4	3	6.5	20
Silicon	0.69	1	1.46	25

In this study, a dual approach combining operando synchrotron XRD measurements with differential capacity plots was employed to perform the first systematic analysis of Gr (de)lithiation dynamics in relation to varying Si:Gr electrode compositions and (dis)charge currents in Si-rich SiGr anodes. Comparative analysis of the structural and electrochemical behavior of SiGr electrodes with two distinct compositions (30 wt.% Si and 70 wt.% Si) against Gr-only electrode enabled differentiation of the dynamics of Si and Gr individual components. High Si content could allow for construction of extremely thin electrodes, and thus good rate performance, even if full utilization of the silicon may not be feasible due to the high expansion. The lower cut-off voltage was kept at 50 mV for most experiments, but also, the impact of the lower cutoff voltage was investigated with respect to the partly overlapping processes of LiC_6 formation, amorphization of residual crystalline Si, and formation crystalline of $Li_{15}Si_4$. The insights gained from this work provide fundamental and general insights that can serve as a basis for the development of optimized Si-rich SiGr electrode design and operation.

2. Experimental Section

2.1. Electrode and Electrolyte Preparation

Gr powder (TIMCAL c-NERGY KS-6L), and high purity Si powder (ReSiTec, RST 15–59) containing <0.2 at.% of metallic impurities were used as active materials. The particle size and surface area of both powders are detailed in **Table 1** and SEM micrographs of the powders can be found in Figure S1 (Supporting Information).

The binder solution was prepared by dissolving Na-alginate (Sigma Aldrich) in an aqueous potassium citrate buffer solution (pH 3) at a solid:liquid ratio = 1:30, which has been shown to enhance the performance of micron-sized Si anodes by promoting esterification and improving bond strength.[25,26] The slurries were prepared by mixing the binder solution with the active materials in a Retsch MM400 mixer mill (f = 25 Hz, duration 45 min). The resulting slurries were then casted onto a customized Cu foil using an RK K control coater. To minimize Cu scattering during XRD acquisition, the Cu foil was perforated with1 mm diameter holes, creating a free-standing electrode area of the same diameter (Figure S4, Supporting Information). Electrode compositions are provided in **Table 2**.

Electrodes of 12 mm diameter were punched from the cast films, ensuring that the perforation was centrally located and uniformly covered by the electrode material. The electrodes were then dried under vacuum at 80 °C for 24 h and stored in an Ar-filled glove box with oxygen and water levels <0.1 ppm. Cross-sectional PFIB-micrographs of the 30% Si and 70% Si electrodes including EDS elemental mapping can be found in Figures S2 and S3 (Supporting Information).

Table 2. Overview of electrode compositional properties and theoretical capacity.

Electrode ID	Binder [wt.%]	Active material [AM, wt.%]	Si:Gr ratio in AM [wt.%]	Electrode mass loading [mg_{AM}/cm^2]	Theoretical capacity [mAh g^{-1}]
100Gr	10	90	0:100	1.12	372
30% Si	10	90	30:70	3.45	1310.4
70% Si	10	90	70:30	1.90	2561.6

Ethylene carbonate (EC), dimethyl carbonate (DMC), and fluoroethylene carbonate (FEC) were supplied by Sigma Aldrich in battery grade purity and used as received. Lithium bis(fluorosulfonyl)imide (LiFSI, 99.9%, Solvionic) was used as electrolyte salt due to its favorable SEI forming properties.[27,28] The electrolyte composition for all cells was a mixture of EC/DMC (1:1 wt.%) + 1M LiFSI + 10 wt.% FEC.

2.2. Cell Assembly and Measurement Procedure

A custom-designed two-electrode electrochemical cell, specifically developed for operando XRD studies of battery systems[29] was employed. Details of the cell structure are provided in Figure S5A (Supporting Information). The cells were assembled in an Ar-filled glove box with the working electrode, an 18 mm diameter polymer separator (Solupor 7P03A) soaked with 60 µL of electrolyte, and a 16 mm Li chip serving both as counter and reference electrode, in contact with a perforated stainless-steel spacer.

Time-resolved operando synchrotron X-ray powder diffraction experiments were conducted at the Swiss-Norwegian beamline BM01 of the European Synchrotron Radiation Facility (ESRF). A monochromatic X-ray beam with wavelength of 0.68995 Å and a size of 300 µm × 300 µm was used, with the electrochemical cell aligned such that its vertical axis was parallel to the incident beam (Figure S5B, Supporting Information). X-ray diffraction patterns were systematically measured at 3 different spots within the free-standing electrode area to check electrode homogeneity upon cycling (Figure S5C, Supporting Information). A 2D Pilatus2M detector was used for data acquisition. Each frame had a collection time of 10 s. Acquisition intervals were set at 1, 2, 3, and 6 min, depending on the applied C-rate. LaB_6 (NIST) was used as calibrant. The raw diffraction data can be retrieved at the ESRF data portal.[30]

Electrochemical cycling was conducted using a PalmSens 4 single channel potentiostat. Each cell underwent an initial formation cycle at C/20, with C referring to the theoretical capacity listed in Table 2. The assumed theoretical capacities were 3500 mAh g^{-1} for pure Si and 372 mAh g^{-1} for Gr. The cells were then cycled for one full charge/discharge cycle at C/5, C/2, 1C, followed by a final C/5 cycle (denoted as C/5-2). The lower cutoff voltage was maintained at 50 mV versus Li/Li^+ for all experiments unless stated otherwise.

2.3. Data Processing

The as-obtained 2D detector images were masked and Azimuthally integrated using the SNBL BUBBLE software to give 1D PXRD patterns.[31] The integrated diffractograms were then fitted in the regions of interest using Gaussian/Lorentzian multiple-peak deconvolution in Python 3 with thoroughly chosen polynomial background functions and peak constraints (peak center, width, and area) to ensure high-quality peak information. Differential capacity (dQ/dV) curves from the raw current and voltage data were obtained based on the method introduced by Thompson et al.,[32] further details of which can be found in the Supporting Information.

3. Results and Discussion

Figure 1 provides a schematic representation of the performed experiments. As a basis for the interpretation of SiGr composite anodes, operando XRD analysis on the (de)lithiation of 100Gr was also conducted, and the corresponding results are shown in Figures S6–S9. Results of operando XRD measurements are shown for 30% Si electrode cycled at C/5, C/2, and 1C, followed by similar analysis on the 70% Si electrode. In the following section, a repetition of C/5 cycle (denoted C/5-2 and performed after the respective 1C cycles) of 30% Si and 70% Si are discussed to unveil structural and electrochemical changes of either electrode resulting from the testing sequence. In the final section, the behavior of the electrodes beyond the previously and consistently used 50 mV lower cutoff potential is presented. For this, the 30% Si and 70% Si electrodes were charged to 0 mV at a C-rate of C/5.

The nomenclature used in this work is as follows: dilute phase 1 corresponds to stage 1L (LiC_{40}), and G1 represents the plateau

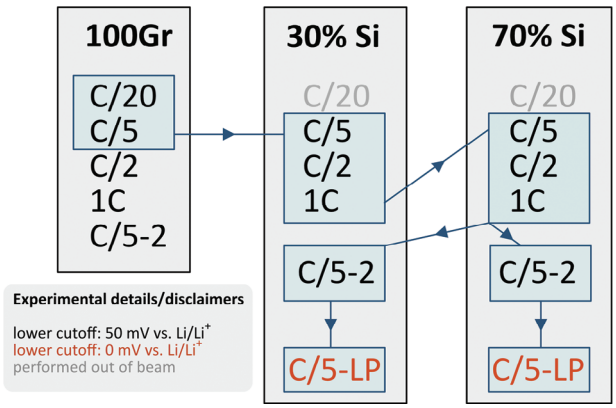

Figure 1. Schematic representation of the scope of the work. Samples are indicated by grey boxes, and the chronological order of operando X-ray measurements is listed from top to bottom. The sequence of presentation within the results section is indicated by the blue boxes and connecting arrows. Individual measurements are color coded according to important experimental details and disclaimers.

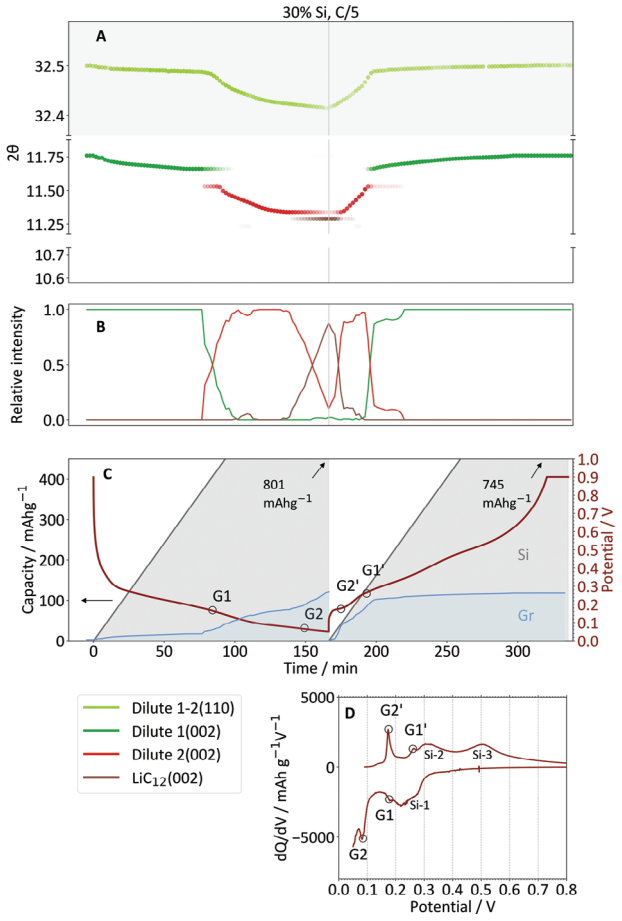

Figure 2. a) Peak position of deconvoluted peaks in Gr (110) region (top, grey shaded) and Gr (002) region (bottom) of a 30% Si electrode cycled at C/5. b) Relative intensities of deconvoluted peaks of Gr (002) region. c) Voltage profile including labelled voltage plateaus. The total charge/discharge capacity is represented by the grey line which goes beyond the scale (final charge/discharge capacities as indicated by arrows). The blue-shaded region represents the capacity provided by Gr, whereas the capacity attributed to Si and side reactions is represented by the grey-shaded region. d) Differential capacity plot.

denoting the transition from stage 1L to dilute phase 2, which is comprised of stage 4L (LiC_{30}) and stage 3L(LiC_{18}).[33] Conversion of 3L (LiC_{18}) to LiC_{12} provokes plateau G2, and plateau G3 denotes the conversion of LiC_{12} to LiC_6.[33] In all the presented data, peak positions of main reflections are shown together with relative peak intensities, corresponding electrode capacity, and differential capacity plots.

3.1. (De) Lithiation Behavior of 30% Si Anode

Figure 2a,b present the operando XRD data for the 30% Si electrode cycled at C/5 based on the diffraction patterns presented in Figure S12. Figure 2c shows the corresponding voltage curve including the total electrode capacity (dark-grey line). Gr volume expansion, calculated from the *a*- and *c*-parameters of the respective GICs, was used to calculate the state of charge of Gr *x* in Li_xC_6 according to the method explained in Section S10. The value of *x* is converted into the capacity provided/consumed by Gr, which is represented by the blue-shaded region in Figure 2c. At 30% Si content, the maximum contribution of Gr to the total electrode capacity is 260.4 mAh g^{-1} (at Li_1C_6, x = 1). The grey-shaded area is the difference of total capacity and Gr capacity, attributed to Si (de)alloying and losses/side reactions. Differential capacity data denoting GIC transitions in Gr and (de)alloying processes in Si is provided in Figure 2d.

First, the sequence and capacity contribution of Gr intercalation and Si alloying is explained and compared to 100Gr at C/5. For a direct comparison of GIC interconversion potentials of 30% Si and 100Gr, see Figure S10a,b.

Gr is in dilute phase 1 during the first half of the lithiation cycle (ca. 80 min) before transitioning to dilute phase 2 at plateau G1, indicated by the shoulder at ca. 180 mV in the differential capacity plot of Figure 2D. At G1, only ca. 25 mAh g^{-1} of the capacity is provided by Gr (corresponding to $x \approx 0.1$ in Li_xC_6), whereas the total electrode capacity is ca. 400 mAh g^{-1}. This illustrates that the alloying of Si dominates at high potentials, as expected, and observed also in other works.[22,34] The capacity contribution of Si is reflected by the broad double-peak feature labeled Si-1 initiated at ≈500 mV in the differential capacity plot. In contrast, the differential capacity of the 100Gr electrode is featureless in this potential region (Figure S9d). The feature Si-1 can be attributed to the formation of $Li_{2.0}Si$[35] from amorphous Si, most of which is produced from the semicrystalline starting material in the preceding C/20 formation cycle performed out of the beam.

Beyond G1, the Gr is lithiated to a more significant extent, which is also accompanied by a more pronounced movement of the Dilute 1–2 (110) peak. As the potential approaches ≈140 mV, the differential capacity shows a sharp peak attributed to the amorphization of residual crystalline silicon[35] which overlays the subsequent GIC peaks. For a closer discussion of the alloying of crystalline Si contained in the 30% Si electrode, the reader is referred to Section 3.4. Concerning Gr, its phase transition to LiC_{12} proceeds at 85 mV, corresponding to the peak G2. In contrast, this transition occurs at 108 mV in the 100Gr C/5 sample (Figure S9a). No LiC_6 signal is detected. The lower SOC of Gr at the end of lithiation ($x \approx 0.46$) as opposed to 100Gr sample is explained by the shift of G2 closer toward the cutoff potential of 50 mV. Consequently, the lack of LiC_6 reflections in the diffraction data as well as electrochemical data is explained by the shift of G3 for which the cutoff potential needs to be <50 mV (see Section 3.5).

At the end of lithiation, a capacity of ≈800 mAh g^{-1} is achieved. This value is lower than the expected theoretical capacity of ≈1310 mAh g^{-1}. This is partly due to the partial utilization of Gr ($x \approx 0.46$) associated with the chosen cutoff voltage of 50 mV, but mostly due to the increased C-rate (C/5) compared to the C/20 formation cycle and the irreversible capacity of the latter. The preceding formation cycle had a lithiation/delithiation capacity of 1210 and 920 mAh g^{-1}, respectively, which is in accordance with previous reports.[36]

In all, the lithiation of Gr is minimal at potentials >260 mV, before competing with the ubiquitous Si lithiation at lower potentials. Interestingly, the delithiation pattern is not just the reversal of the lithiation. It is evident that the delithiation voltage curve presents a large overpotential. This effect is attributed to the (de)alloying reaction of Si, which has much higher hysteresis

compared to Gr (de)intercalation.[37] Accordingly, the two transitions G2' (180 mV) and G1' (260 mV) occur over a rather short time span and almost all the electrode capacity at the beginning of the delithiation cycle stems from Gr, with only a small contribution of Si dealloying. In fact, almost complete delithiation of the graphite (110 mAh g^{-1}) is observed after ≈200 min. This observation is in close agreement with a recent study of Heubner et al.[37] that used isolated Gr/Li and Si/Li half cells connected in parallel, which allowed them to observe and deconvolute the separate contribution of Si and Gr to the charge storage. In our study, we demonstrate for the first time that the same delithiation pattern is observed in an actual composite electrode, where mutual interaction of individual components must be expected.

After passing G1', Gr is almost completely delithiated, and its capacity contribution is negligible. The remaining electrode capacity of the delithiation cycle (ca. 680 mAh g^{-1}) is exclusively provided by Si: Peak Si-2 denotes the delithiation of highly lithiated amorphous Si ($Li_{3.5}Si \rightarrow Li_{2.0}Si$), followed by the recovery of amorphous Si ($Li_{2.0}Si \rightarrow$ a-Si) indicated by peak Si-3.[35]

It should be noted that the specific currents defined by the cycling rate C/5 are much higher for the 30% Si electrode compared to 100Gr (262 vs 74 mA g^{-1}, respectively). Indeed, the shift of the G2 and G2' peaks resemble reasonably well the polarization observed for the 100Gr electrode at 1C (Figure S10a,b), run at a comparable specific current of 370 mA g^{-1}. Therefore, we argue that the high specific currents encountered in SiGr composites challenge the rate capability of Gr, and that specific currents, instead of a nominal C-rate, can be a more appropriate measure of the current load that Gr is subjected to.

The fact that LiC_{12} is the most lithiated GIC and that LiC_6 is absent in both the electrochemical and diffraction data is in good agreement with a study of Yang et. al, in which a 50% Si electrode attained "lithiated Gr with stage index 2". (≙ LiC_{12}) upon lithiation, even at a substantially lower C-rate (C/27) and a cut-off voltage of 5 mV.[20] Also, LiC_{12} is only detected at one measured spot on the electrode, whereas the 100Gr electrode at C/5 presents LiC_{12} in the diffraction data (and LiC_6 as G3 peak in the differential data in Figure S9d), again underlining the lower SOC of Gr in the composite electrode.

The (de)lithiation behavior of the 30% Si electrode at higher C-rates is presented in **Figure 3**.

Comparing C/5 (Figure 2) with C/2 and 1C (Figure 3), it is evident that a higher C-rate decreases the maximum SOC of Gr: While LiC_{12} was present at C/5, the highest lithiated GIC at C/2 and 1C is dilute phase 2, and the minimum value of 2θ at the end of lithiation increases from 11.35° to 11.45°, respectively. The Gr's share of lithiation capacity amounts to 70 mAh g^{-1} ($x \approx 0.26$) and 50 mAh g^{-1} ($x \approx 0.19$) at C/2 and 1C, respectively, and most of it is released at the beginning of the delithiation cycle. The lower SOC of Gr and its preferential capacity contribution upon initial delithiation is again explained by the increase of polarization (Figure S10b, Supporting Information). The development of the potential of G1 (G1') at C/5, C/2, and 1C is: 180 mV (260 mV), 150 mV (290 mV), and 80 mV (320 mV) versus Li/Li^+. The absence of LiC_{12} from C/2 onward can be explained by a G2 potential shifting to values beyond the 50 mV versus Li/Li^+ cutoff potential.

Results shown in Figure 3 are indicative of preferential lithiation of amorphous Si at high potentials, competing lithiation of Gr and Si at low potentials, followed by preferential delithiation of Gr, and delithiation of amorphous lithium silicide. Lithium plating, which is detectable with operando XRD[38] and is promoted in SiGr anodes exposed to high rates,[39] was not be evidenced.

3.2. (De) Lithiation Behavior of 70% Si Anode

The 70% Si electrode was first subjected to a C/20 formation cycle out of the beam, with lithiation and delithiation capacities of 1960 and 1695 mAh g^{-1}, respectively. The cell was then placed under the beam to perform a lithiation/delithiation cycle at C/5. **Figure 4a–d** shows the obtained results. The corresponding X-ray diffraction patterns can be found in Figure S13.

Similar to the 30% Si sample, Gr remains in dilute phase 1 for about the first half of the lithiation cycle (ca. 90 min). The electrode capacity up to G1 (ca. 750 mAh g^{-1}) is primarily provided by amorphous Si alloying, denoted by Si-1. The process G1 does not appear as distinct peak in the differential capacity plot due to the low amount of Gr in the electrode and the overlapping signal of the process Si-1. The potential value of G1 estimated from diffraction data is 170 mV, which is in close resemblance to 30% Si at C/5 (Figure 2; Figure S10b,c, Supporting Information).

Compared to 100Gr and 30Si at C/5, there are several indications that lithium diffusion in Gr becomes increasingly inhibited with increasing Si content: First, the evolution of the dilute phase 1 peak position with time (green curve in Figure 4a) exhibits a convex shape, as opposed to a concave shape as observed in 100Gr and 30% Si samples. Second, clear changes among 100Gr, 30%Si, and 70% Si are seen in the Gr(002) peak shape during G1 transition: While the full width of half maximum (FWHM) is of 0.18 for 100Gr, it increases to 0.25 and to 0.45 for 30%Si and 70% Si, respectively, with the appearance of distinct shoulders (Figure S14). This suggests that the GICs coexist for a longer timespan before they are converted into another, which can be due to blocked lithium diffusion owing to Si expansion.

Upon further lithiation, the formation of LiC_{12} (indicated by G2) occurs at ca. 85 mV as derived from the diffraction data. Notably, the potentials of G1 and G2 do not differ between 30% Si C/5 and 70% Si C/5 samples, even though the specific current of latter is 1.9-fold of the former. This illustrates that the specific current is not the only decisive factor for the polarization of the Gr. In fact, the SOC of Gr in the 70% Si C/5 electrode is slightly higher than in the 30% Si C/5 electrode: The lower-intensity LiC_{12}(300) peak is detected in Figure 4a, whereas it is absent in the 30% Si electrode (Figure 2a), implying that the contribution from Gr is ≈55 mAh g^{-1} ($x \approx 0.5$). The slightly higher SOC of Gr in 70% Si compared to 30% Si at C/5 is not straightforward to explain as the GIC potentials do not differ. This could be explained by more severe Si particle cracking in the 70% Si electrode, which could result in a higher fraction of inactive Si than in the 30% Si electrode, therefore increasing the propensity of Gr lithiation. It should also be noted that the Li diffusion coefficient is expected to be higher in graphite than in Silicon (1.2×10^{-16} m^2 s^{-1} for Si, vs 1.4×10^{-13} m^2 s^{-1} for Gr, for similar materials as used in this study, as estimated in.[40] Differences in Li-diffusion properties was also suggested to be the reason for differences in Gr lithiation kinetics, as well as Li-plating, for graphite-silicon composite electrodes with two different Si materials.[41] Another reason

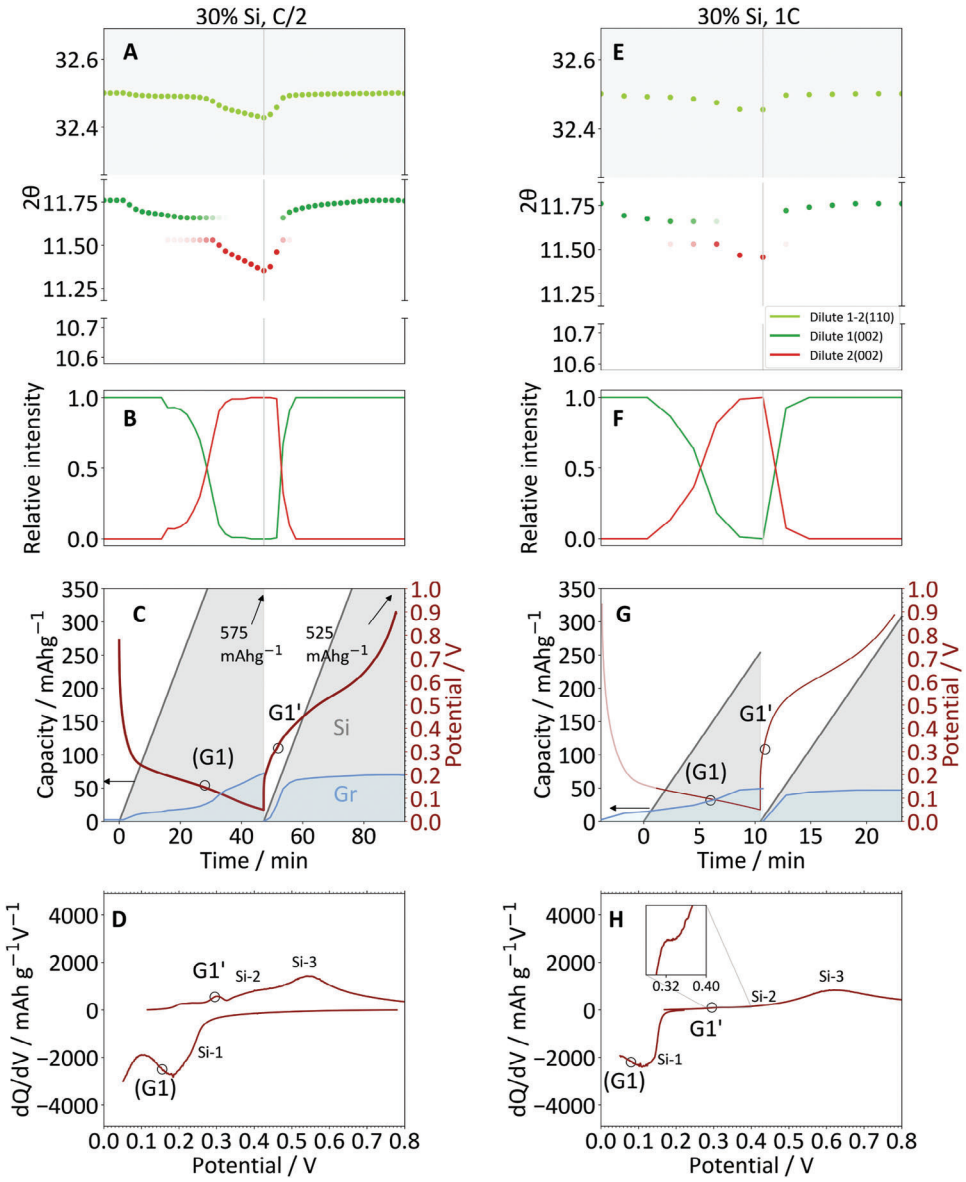

Figure 3. Operando XRD plots, voltage profile, and differential capacity plots of a 30% Si electrode cycled at a–d) C/2 and e–h) 1C. Relevant peaks in differential capacity plots denoting transition of GICs are highlighted. Estimates for GIC transitions based on the diffraction data (without a clear feature in differential capacity) are shown in parentheses. The initial part of the 1C lithiation curve was not captured at the beamline and has been replaced with a lab-made coin cell cycled at identical conditions.

could be local inhomogeneity of the electrode lithiation degree owing to local differences in resistivity.

The delithiation of Gr is indicated by G1' and G2'. However, the Gr capacity contribution is very small in the earliest stages of delithiation. This effect might be a limitation of the procedure used for the Gr SOC calculation in which the relative peak intensities are approximated as phase percentages (see Section S10, Supporting Information). Another explanation for the observed "gap" is crosstalk between Si and Gr, which indeed has been reported in other studies.[39,40,16] These include the transfer of Li^+ from Gr to Si during relaxation,[16,39] or Li^+ crosstalk between silicon and graphite at the end of the charging step.[34] However, such a crosstalk of Li^+ from Si to Gr (which cancels the Li^+ flow out of Gr) can be considered unlikely here, as it proceeds against the net driving force imposed by the discharge current.

The operando XRD plots of 70% Si electrode subjected to C/2 and 1C are shown in **Figure** 5a–d and Figure 5e–h, respectively. Analogous to 30% Si and 100Gr, the rate capability limitation of Gr results in a lower volume expansion as the current is increased: the minimum value of 2θ for dilute 2(002) is 11.37° at C/2 and 11.52° at 1C. This corresponds to a capacity contribution of Gr of 25 mAh g^{-1} ($x \approx 0.22$) and 13 mAh g^{-1} ($x \approx 0.11$), respectively. The negligible capacity contribution in the latter case illustrates that Gr mainly acts as an electron conductor, given the very high specific current of 2560 mA g^{-1}. About 690 mAh g^{-1} of

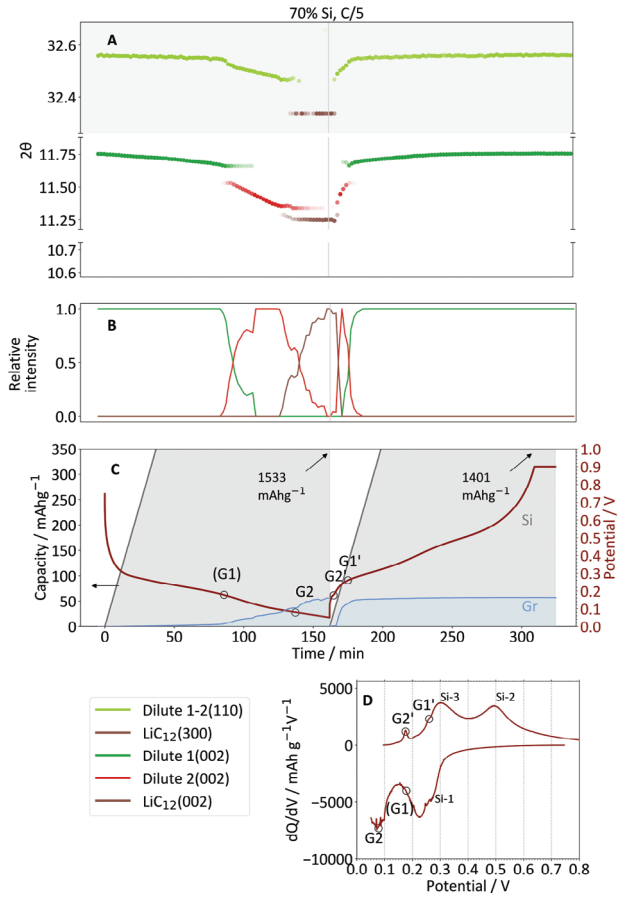

Figure 4. a) Peak position of deconvoluted peaks in Gr (110) region (top, grey shaded) and Gr (002) region (bottom) of a 70% Si electrode cycled at C/20 (formation cycle). b) Relative intensities of deconvoluted peaks of Gr (002) region. c) Voltage profile including labeled voltage plateaus (brackets if determined from XRD data). The total charge/discharge capacity is represented by the grey line. The blue-shaded region represents the capacity provided by Gr, whereas the capacity attributed to Si and losses is represented by the grey-shaded region. d) Differential capacity plot.

the delithiation capacity at 1C is exclusively provided by Si. Even though Gr is negligibly involved in charge storage, the volume buffering effect might still justify the practicality of 70% Si electrodes operated at high currents. In both C/2 and 1C, the absence of LiC_{12} is evidenced by its shift to beyond the lower cutoff potential of 50 mV.

3.3. Impact of C-Rate Testing on Gr and Si Degradation

After the C-rate testing procedure, a second C/5 cycle (C/5-2) was performed to evaluate potential degradation of Si and Gr. The operando XRD plots are shown in Figure S15. For 70% Si, the total electrode lithiation (delithiation) capacity drops from 1533 (1401) at C/5 to 1403 (1333) mAh g^{-1} at C/5-2. For 30% Si, the total electrode lithiation (delithiation) capacity drops from 800 (745) at C/5 to 697 (650) mAh g^{-1} at C/5-2. Despite the drop in total capacity, multiple indicators suggest that Gr sustained no significant structural damage between C/5 and C/5-2 cycles: First, the GIC potentials remain constant for both 30% Si and 70% Si electrodes. Second, the Gr SOC upon the end of lithiation cycle remains at $x \approx 0.49$ in the 70% Si electrode, whereas a slight increase from $x \approx 0.45$ to $x \approx 0.5$ is observed for the 30% Si electrodes. The unexpected, slight increase in Gr SOC might be explained by local inhomogeneities of the electrode, perhaps caused by structural rearrangement of the active material. Third, the peak width between the first diffractogram of C/5 and the last diffractogram of C/5-2 is minor (<3%) for both 30% Si and 70% Si. According to the Debye-Scherrer relation, this suggests that the Gr crystallite sizes remained unchanged. Overall, results illustrate that the high mechanical strain associated with Si expansion, even at 70% Si, has a low impact on the Gr integrity. Instead, the observed capacity fade is almost exclusively attributable to the degradation of Si.

3.4. Lithiation Behavior of Crystalline Si

Operando diffraction data coupled with differential capacity plot of 30% Si at C/5 (Figure 2), indicate that amorphous Si would be first lithiated at ca. 400 mV (indicated by Si-1) to form amorphous Li_xSi. Amorphization of residual Si crystallites upon lithiation can be tracked by the attenuation of Si(111) reflection. **Figure 6** displays the intensity evolution of the Si(111) peak for C/5, C/2, 1C, and C/5-2 cycles of the 30% Si electrode.

At C/5, it is observed that amorphization of crystalline Si commences at ca. 110 mV. Previous works on Si-only electrodes reported an onset potential of 170[35] or 180 mV[42] versus Li/Li^+ for this process. The lower potential in our work is attributed to the higher C-rate, which induces kinetic hindrance and polarization effects. The constant intensity of Si(111) during the delithiation cycles is expected as amorphous lithium silicide dealloying does not produce new amorphous Si. For the higher C-rates of C/2 and 1C, the Si(111) signal remains constant. In the C/5-2 cycle, the current is low enough to induce further Si lithiation, which causes further decrease of Si(111) reflection, implying that the alloying reaction extends to pristine, unreacted crystalline domains of the Si particles. It is widely accepted that µm-sized Si particles form an outer layer of amorphous lithium-silicide upon alloying with lithium, while retaining a crystalline core.[35,43]

The suppression of Si amorphization at C/2 and 1C reveals a promising operation strategy toward stable SiGr anodes for high power applications, since maintaining a crystalline Si core and preventing further Si amorphization has shown to significantly enhance electrode cycle life. For purely Si-based electrodes, cutoff potentials above 170 mV (at a C-rate of C/120) are recommended to prevent Si total amorphization.[35] However, such cutoff potential is impractical for SiGr anodes since Gr would be hardly lithiated. The findings of this study indicate that a lower cutoff potential of 50 mV is feasible under high-power conditions (≥ C/2), effectively minimizing or preventing consumption of crystalline Si. At relatively lower C-rates (≤ C/5), continuous amorphization appears to be inevitable. Nevertheless, the significantly higher Gr utilization under these conditions might compensate for the expected earlier degradation of Si to a certain extent.

In the 70% Si electrode, the absence of Si(111) reflection following the C/20 formation cycle (i.e., first diffraction pattern of

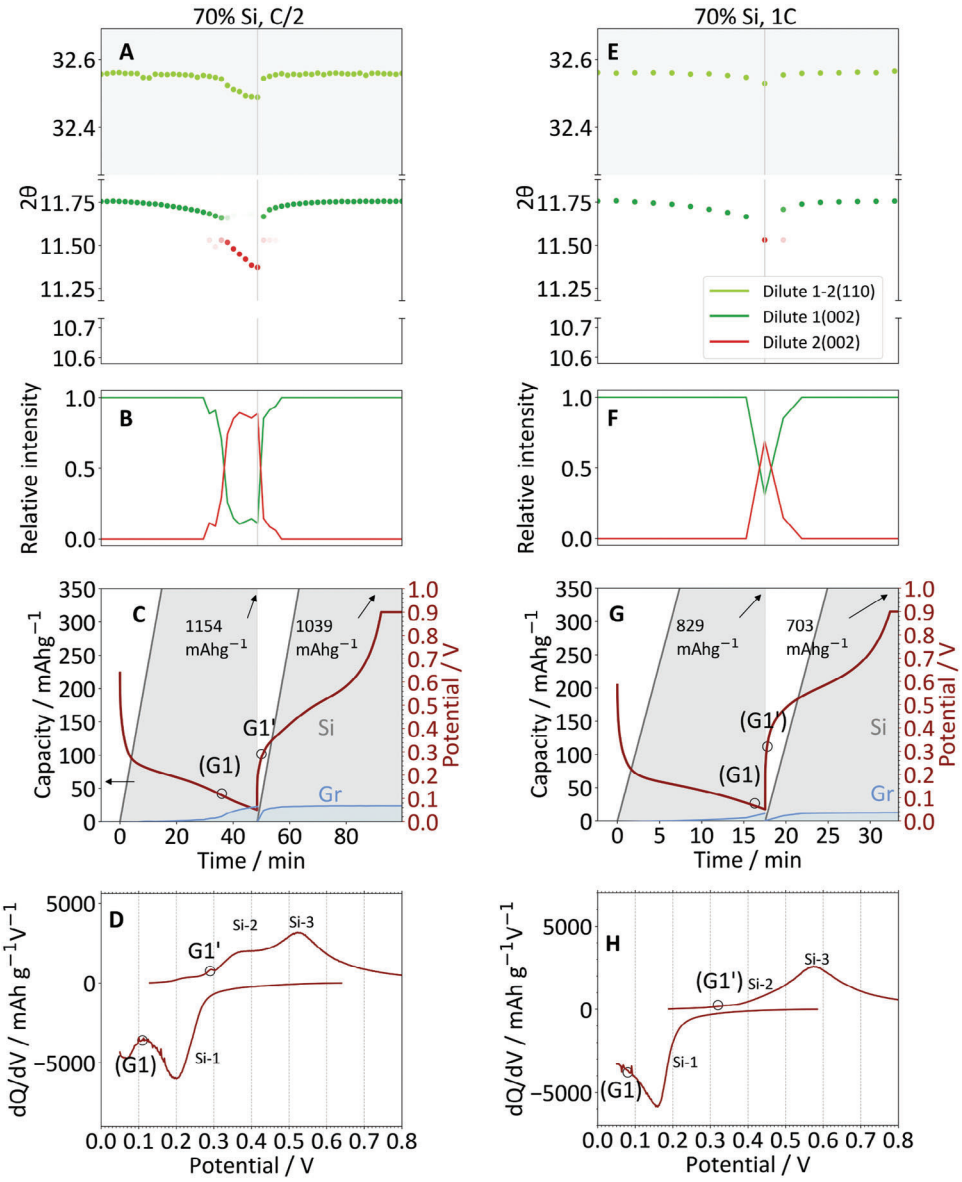

Figure 5. Operando XRD plots, voltage profile, and differential capacity plots of a 70% Si electrode cycled at a–d) C/2 and e–h) 1C. Relevant peaks in differential capacity plots denoting transition of GICs are highlighted. Estimates for GIC transitions based on the diffraction data are highlighted in brackets.

C/5) indicates that all crystalline Si has undergone amorphization. Also, the emergence of $Li_{15}Si_4$ (220) and $Li_{15}Si_4$(310) peaks during the C/5 cycle are observed (Figure S13, Supporting Information). The mechanism behind the complete amorphization in the 70% anode, as opposed to the incomplete amorphization seen in the 30% electrode could be related to the differences in electrode porosity and spatial arrangement of Si and graphite.[44] Based on the cross-section PFIB micrographs (Figures S2 and S3, Supporting Information), the porosity of the pristine 70% Si electrode is significantly lower than in the pristine 30% Si electrode, since the (sub-)micron-sized Si particles fill the voids created by the larger flake-shaped Gr particles. In the 30% Si electrode, some cavities between Gr particles exist, which seem to be sparsely occupied by Si particles. Therefore, Si particles in the 30% Si electrode tend to be segregated by Gr, whereas there is a much more intimate contact between Si particles in the 70% Si electrode. The better percolation in case of 70% Si electrode may therefore facilitate the complete conversion of c-Si (with partial formation of $Li_{15}Si_4$) during the formation cycle, whereas the segregation of Si particles in the 30% Si electrode results in the incomplete amorphization of Si.

In summary, the 70% Si anode exhibits complete Si amorphization and $Li_{15}Si_4$ formation, both known to adversely affect cycling stability. Conversely, the 30% Si electrode retains a stable crystalline Si residue even at high C-rates, indicating its potential suitability for high-power applications.

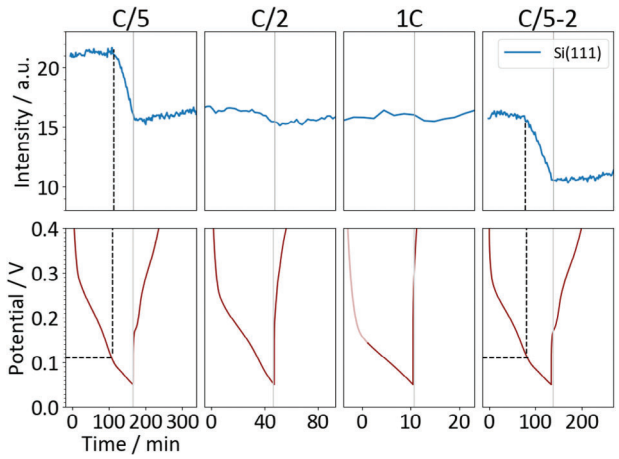

Figure 6. Intensity of Si(111) peak (top) and voltage curves (bottom) for the 30% Si electrode cycled at C/5, C/2, 1C, and C/5-2.

3.5. Extending the Lower Cutoff Voltage: Maximizing Gr Lithiation versus $Li_{15}Si_4$ Formation

The presented findings indicate that Gr is not fully utilized ($x \leq 0.5$) when the lower cutoff voltage is set at 50 mV. To increase Gr lithiation and evaluate any potential interference from side reactions/Si phase transitions, the cutoff potential was further reduced to 0 mV and 30% Si and 70% Si electrodes were subjected to an additional C/5 charge cycle (labeled C/5-LP) after the C/5-2 cycle. In this case, the 0 mV cutoff potential was held for 150 min. An excerpt of the operando diffraction data of the 30% Si electrode and its voltage curve is presented in **Figure 7** (selected raw diffractograms are available in Section S17).

Gr attains its fully lithiated state (LiC_6) as the electrode potential is lowered and held at 0 mV. Simultaneously, all the remaining crystalline Si is amorphized. Also, new peaks are detected, attributable to $Li_{15}Si_4$,[24,45] which is known to form upon strong lithiation of Si and at electrode potentials ≤50 mV in pure Si-based anodes. Its formation should be avoided since it leads to high irreversible capacity.[24]

To further illustrate the different buildup/depletion processes of Gr and Si phases and their respective allocation to the electrode potential, the diffraction peaks for the 30% Si and 70% Si electrodes were deconvoluted and are presented in **Figure 8**. For $Li_{15}Si_4$, the (220) reflection is chosen as representative since it is the highest intensity signal.

For both 30% Si and 70% Si, the LiC_6 phase (indicated by G3) is formed at 40 mV and below, i.e., its formation was not possible in all the previously presented measurements when a cutoff voltage of 50 mV was chosen. For perspective, the differential capacity of the 100Gr anode at C/5 (Figure S9d, Supporting Information) indicated LiC_6 formation at 78 mV.

Expectedly, the Gr lithiation below 50 mV is accompanied by a strong decline in Si(111) intensity for the 30% Si electrode. Long-term cycling at C/5, especially combined with a cutoff voltage <50 mV in favor of full Gr utilization appears to inevitably result in full amorphization. The 70% Si electrode has no remaining crystalline Si left after formation cycle, as stated earlier.

The formation of $Li_{15}Si_4$ is different between the 30% and 70% Si electrodes: In the 30% Si electrode, its formation does not occur before the voltage hold step at 0 mV. In the 70% Si electrode, a small amount of $Li_{15}Si_4$ starts forming from ≈30 mV. The delayed formation of $Li_{15}Si_4$ in the first case might be due to the residual crystalline Si, which first needs to be fully converted into a-Li_xSi before the crystallization of $Li_{15}Si_4$ can occur. The slightly earlier onset of $Li_{15}Si_4$ in 70% Si is consistent with the observed higher tendency of Si amorphization, since Si requires a very high degree of lithiation before $Li_{15}Si_4$ is formed.[24] For both 30% Si and 70% Si, the onset potential of $Li_{15}Si_4$ formation is significantly lower than the established value of 50 mV for silicon-only electrodes cycled at very slow C-rates of C/90 [24] and C/100.[46] This can be partly attributed to the rather high C-rate of C/5.

4. Perspectives for Optimized Cycling Conditions SiGr Anodes

The findings on the capacity contribution of Li_xC_6 and a-Li_xSi and the potential- and composition-dependent amorphization of c-Si, can serve to provide recommendations for the performance optimization of SiGr electrodes. First, a viable application lies in the potential-controlled shallow cycling of SiGr anodes. Setting a cutoff potential of 50 mV would lead to an initial capacity increase followed by drastic capacity fade due to the continuous depletion of c-Si. Instead, by increasing the cutoff at values above the detected c-Si amorphization threshold potential of 110 mV at a C-rate of C/5 (see Figure 6) can, higher capacity retention can be achieved. Conversely, an alternative approach is to increase the current, while keeping the lower cutoff at 50 mV. As demonstrated in Figure 6, the 30% Si electrode cycled at C/2 presents a constant intensity of Si(111), implying that c-Si is not further amorphized. Thereby, stable long-term cycling is expected, despite a cutoff potential of 50 mV.

Second, the shallow cycling of SiGr anodes opens possibilities for use in devices such as Li-ion capacitors. Through pre-lithiation to a target SOC and shallow cycling in a narrow capacity regime, the extent of electrochemical activity of Gr and Si can be precisely tailored, which expectedly allows to balance energy density against long-term stability. For example, pre-lithiation of the SiGr anode to a potential of 40 mV and subsequent shallow cycling involves Gr to a large extent and the low operating potential regime enables a high cell voltage. Shallow cycling in such a low potential regime, however, bears the drawbacks of continuous Si amorphization of c-Si, the formation of $Li_{15}Si_4$, as well increased probability of Li plating. In contrast, pre-lithiation to a potential of 300 mV with subsequent shallow cycling would exclusively involve Si without any contribution of Gr, at cost of a lower cell voltage (and therefore a lower energy density). Shallow cycling in a higher potential regime would also greatly reduce the risk of Li plating, and the prevention of the continuous Si amorphization (which occurs <110 mV at C/5) promises good cycling stabilities. Further studies will investigate the impact of the potential regime on long-term stability under shallow cycling conditions of SiGr anodes.

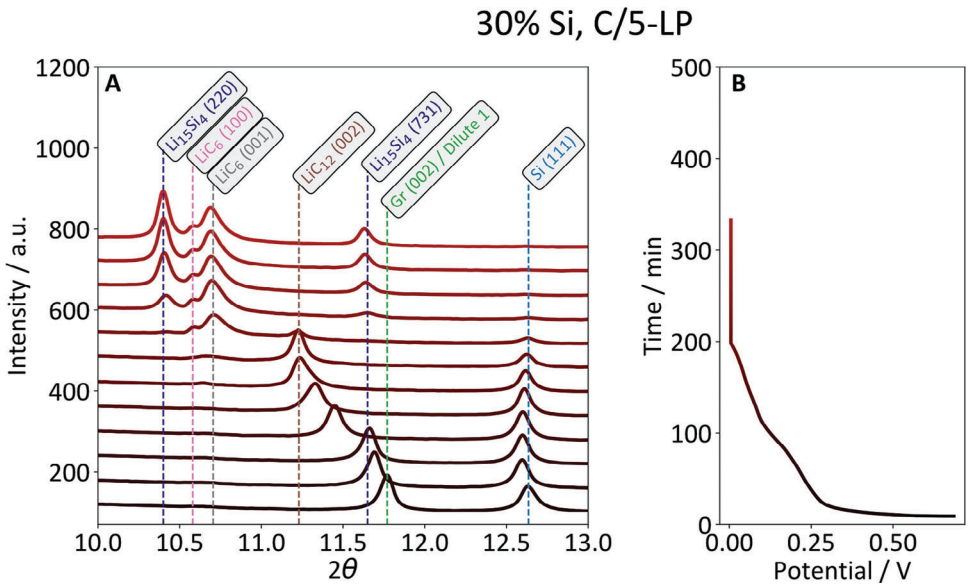

Figure 7. a) Operando XRD patterns of the 30% Si electrode charged to and held at 0 mV. b) Voltage profile.

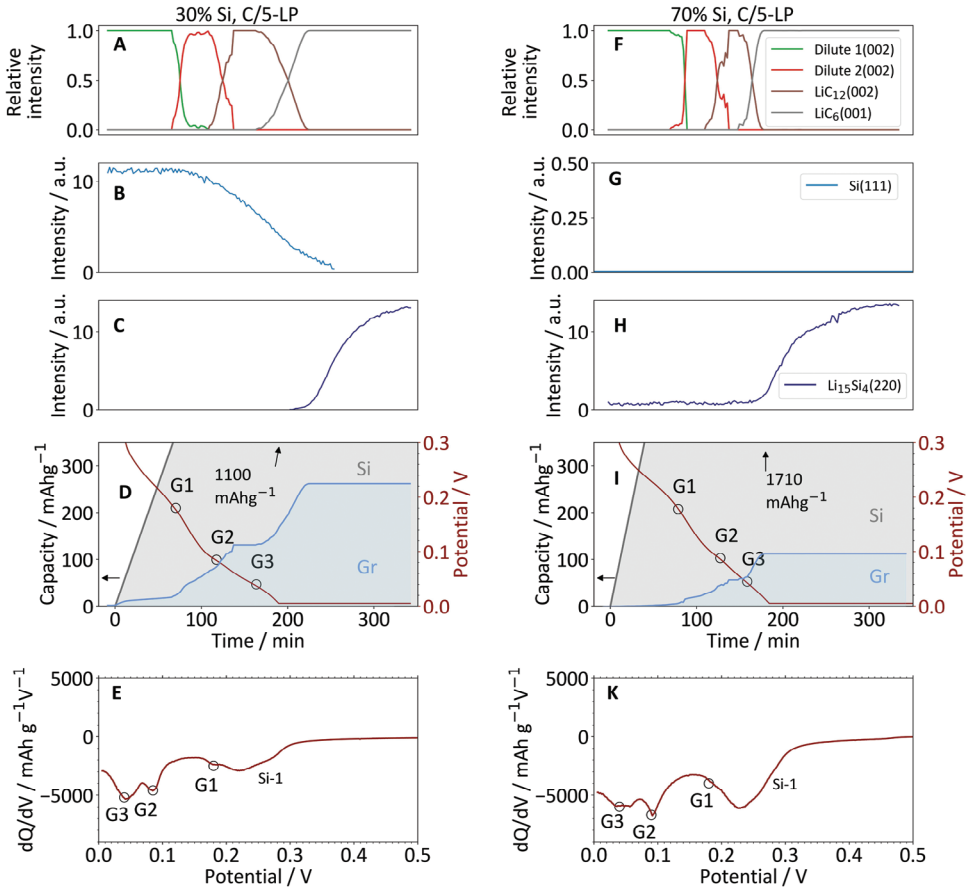

Figure 8. Operando XRD and electrochemical data for 30% and 70% Si electrodes charged to 0 mV at C/5 and held at 0 mV. a,f) Relative intensities of selected deconvoluted GIC peaks. b,g) Evolution of Si(111) peak intensity. c,h) evolution of $Li_{15}Si_4$(220) peak intensity. d,i) Voltage profile (magnified to display the relevant potential range) and capacity share of Gr and Si. e,k) Differential capacity plots.

5. Conclusion

This study has elucidated critical aspects of the lithiation and delithiation mechanisms in SiGr composite anodes containing 30 and 70 wt.% Si cycled at various C-rates. For both compositions, the principal (de)lithiation sequence is as follows: 1) above ≈200 mV versus Li/Li^+, a-Si is preferentially lithiated with negligible Gr utilization. 2) Below ≈200 mV versus Li/Li^+, both Gr, and a-Si, along with residual c-Si, undergo competitive lithiation. 3) During the initial stage of delithiation, the capacity is primarily derived from Gr, with minimal contribution of Si due to its high delithiation overpotential. 4) Following complete Gr delithiation, the delithiation of a-Li_xSi takes place.

The study also highlights rate capability limitations for Si-rich SiGr anodes. High specific currents in SiGr anodes induce a downward shift in the interconversion potentials of GIC. At a 50 mV cutoff potential and a C-rate of C/5, Gr in both the 30 and 70 wt.% Si electrodes attain a lower SOC compared to graphite-only (100Gr) electrode. To maximize Gr's SOC in SiGr anodes, the cutoff potential must be set lower than the 50 mV versus Li/Li^+ typically used for Si-only electrodes. Despite the expected mechanical stress resulting from Si volume changes upon cycling, no significant deterioration in Gr's structural integrity was observed, indicating that capacity fade can be primarily attributed to Si degradation.

Significantly differences between 30 and 70 wt.% Si electrodes. In the 70 wt.% Si electrode, complete Si amorphization and the formation of crystalline $Li_{15}Si_4$ phase during the formation cycle is observed, provides solid evidence of critical challenges to achieve long-term stability of Si-rich SiGr anodes. In contrast, the 30 wt.% Si electrode undergoes only partial amorphization during the formation cycle, with no signals of crystalline $Li_{15}Si_4$ formation. Notably, the resistance of c-Si's to further amorphization at C-rates ≥C/2 may enhance Si particle stability, thereby extending the cycle life of SiGr anodes under high-power conditions.

The current- and potential-dependent quantification of capacity contributions from Gr and Si components presented in this study offers a framework for the precise tailoring and operation of on Si-rich SiGr anodes. By employing shallow cycling within specific anode potential regimes, the electrochemical activity of Si and Gr could be controlled, potentially prolonging the cycle life of SiGr anodes by limiting Si's volumetric changes.

Supporting Information

Supporting Information is available from the Wiley Online Library or from the author.

Acknowledgements

Dr. Vadim Dyadkin (BM01 SNBL) is kindly acknowledged for local support at the beamline during conduction of the experiments, raw data acquisition and treatment. P.S. gratefully acknowledges financial support of this work by the Research Council of Norway (contract number 306400) within the project "Norwegian Giga Battery Factories (NorGiBatF)". M.V.B and W.H. acknowledge the Norwegian Research Council (contract number 315947). P.A.S. acknowledges Grants No. PCI2022-132993 funded by MCIN/AEI/10.13039/501100011033 and DGA/M4 from Diputación General de Aragón. Dr. Hamid Khanmohammadi is gratefully acknowledged for performing cross-sectional micrographs and EDS of SiGr electrodes at the NTNU-PFIB lab, which is part of the SMART-H Infrastructure, supported by the Research Council of Norway (project 296197) and NTNU.

Conflict of Interest

The authors declare no conflict of interest.

Data Availability Statement

The data that support the findings of this study are openly available in Repository name at https://doi.org/10.15151/ESRF-ES-780223200[DOI], reference number [780223200].

Keywords

capacity share, cutoff potential, graphite, high power cycling, operando X-ray diffraction, polarization, silicon

Received: August 8, 2024
Revised: September 18, 2024
Published online: October 9, 2024

[1] H. Zhang, Y. Yang, D. Ren, L. Wang, X. He, *Energy Storage Mater.* **2021**, *36*, 147.
[2] C. Wang, C. Yang, Z. Zheng, *Adv. Sci.* **2022**, *9*, 2105213.
[3] J. Cho, *J. Mater. Chem.* **2010**, *20*, 4009.
[4] A. Casimir, H. Zhang, O. Ogoke, J. C. Amine, J. Lu, G. Wu, *Nano Energy* **2016**, *27*, 359.
[5] A. F. Gonzalez, N.-H. Yang, R.-S. Liu, *J. Phys. Chem. C.* **2017**, *121*, 27775.
[6] Y. Sun, N. Liu, Y. Cui, *Nat. Energy.* **2016**, *1*, 16071.
[7] S. Chae, S. Choi, N. Kim, J. Sung, J. Cho, *Angew. Chem., Int. Ed.* **2020**, *59*, 110.
[8] P. Li, H. Kim, S.-T. Myung, Y.-K. Sun, *Energy Storage Mater.* **2021**, *35*, 550.
[9] A. Ghamlouche, M. Müller, F. Jeschull, J. Maibach, *J. Electrochem. Soc.* **2022**, *169*, 020541.
[10] M. Wetjen, D. Pritzl, R. Jung, S. Solchenbach, R. Ghadimi, H. A. Gasteiger, *J. Electrochem. Soc.* **2017**, *164*, A2840.
[11] F. Jeschull, Y. Surace, S. Zürcher, G. Lari, M. E. Spahr, P. Novák, S. Trabesinger, *J. Electrochem. Soc.* **2020**, *167*, 100535.
[12] E. Moyassari, T. Roth, S. Kücher, C.-C. Chang, S.-C. Hou, F. B. Spingler, A. Jossen, *J. Electrochem. Soc.* **2022**, *169*, 010504.
[13] M. K. S. Verma, R. S. Patil, S. Bharathraj, S. P. Adiga, K. S. Mayya, *Electrochim. Acta.* **2023**, *448*, 142105.
[14] B. Shi, B. Han, H. Xie, Y. Kang, Q. Zhang, *Electrochim. Acta.* **2021**, *378*, 138151.
[15] J. Choi, G. Kim, S. Y. Kim, *Energy Technol.* **2023**, *11*, 2201444.
[16] D. P. Finegan, A. Vamvakeros, L. Cao, C. Tan, T. M. M. Heenan, S. R. Daemi, S. D. M. Jacques, A. M. Beale, M. Di Michiel, K. Smith, D. J. L. Brett, P. R. Shearing, C. Ban, *Nano Lett.* **2019**, *19*, 3811.
[17] S. Tardif, E. Pavlenko, L. Quazuguel, M. Boniface, M. Maréchal, J.-S. Micha, L. Gonon, V. Mareau, G. Gebel, P. Bayle-Guillemaud, F. Rieutord, S. Lyonnard, *ACS Nano* **2017**, *11*, 11306.
[18] C. L. Berhaut, D. Z. Dominguez, P. Kumar, P.-H. Jouneau, W. Porcher, D. Aradilla, S. Tardif, S. Pouget, S. Lyonnard, *ACS Nano* **2019**, *13*, 11538.
[19] H. Jung, K. S. Kim, S.-E. Park, J. Park, *Electrochim. Acta.* **2017**, *245*, 791.

[20] X. Q. Yang, J. McBreen, W. S. Yoon, M. Yoshio, H. Wang, K. Fukuda, T. Umeno, *Electrochem. Commun.* **2002**, *4*, 893.
[21] C.-W. Hu, J.-P. Chou, S.-C. Hou, A. Hu, Y.-F. Su, T.-Y. Chen, W.-K. Liew, Y.-F. Liao, J.-L. Huang, J.-M. Chen, C.-C. Chang, *Sci. Rep.* **2019**, *9*, 1299.
[22] K. P. C. Yao, J. S. Okasinski, K. Kalaga, J. D. Almer, D. P. Abraham, *Adv. Energy Mater.* **2019**, *9*, 1803380.
[23] J. Park, S. S. Park, Y. S. Won, *Electrochim. Acta.* **2013**, *107*, 467.
[24] M. N. Obrovac, L. Christensen, *Electrochem. Solid-State Lett.* **2004**, *7*, A93.
[25] D. Mazouzi, Z. Karkar, C. Reale Hernandez, P. Jimenez Manero, D. Guyomard, L. Roué, B. Lestriez, *J. Power Sources* **2015**, *280*, 533.
[26] B. Bitsch, J. Dittmann, M. Schmitt, P. Scharfer, W. Schabel, N. Willenbacher, *J. Power Sources* **2014**, *265*, 81.
[27] B. Philippe, R. Dedryvèire, M. Gorgoi, H. Rensmo, D. Gonbeau, K. Edström, *J. Am. Chem. Soc.* **2013**, *135*, 9829.
[28] K. Asheim, P. E. Vullum, N. P. Wagner, H. F. Andersen, J. P. Mæhlen, A. M. Svensson, *RSC Adv.* **2022**, *12*, 12517.
[29] O. A. Drozhzhin, I. V. Tereshchenko, H. Emerich, E. V. Antipov, A. M. Abakumov, D. Chernyshov, *J. Synchrotron Radiat.* **2018**, *25*, 468.
[30] M. V. Blanco, F. Cova, W. Hua, C. Lian, I.-E. Nylund, P. Schweigart, *Eur. Synchrotron Radiat. Facil.* **2025**, https://doi.org/10.15151/ESRF-ES-780223200.
[31] V. Dyadkin, P. Pattison, V. Dmitriev, D. Chernyshov, *J. Synchrotron Radiat.* **2016**, *23*, 825.
[32] N. Thompson, T. Cohen, S. Alamdari, C.-W. Hsu, G. Williamson, D. Beck, V. Holmberg, *J. Open Source Softw.* **2020**, *5*, 2624.
[33] C. Schmitt, A. Kube, N. Wagner, K. A. Friedrich, *ChemElectroChem* **2022**, *9*, 43.
[34] J. Moon, H. C. Lee, H. Jung, S. Wakita, S. Cho, J. Yoon, J. Lee, A. Ueda, B. Choi, S. Lee, K. Ito, Y. Kubo, A. C. Lim, J. G. Seo, J. Yoo, S. Lee, Y. Ham, W. Baek, Y.-G. Ryu, I. T. Han, *Nat. Commun.* **2021**, *12*, 2714.
[35] M. Graf, C. Berg, R. Bernhard, S. Haufe, J. Pfeiffer, H. A. Gasteiger, *J. Electrochem. Soc.* **2022**, *169*, 020536.
[36] M. Cabello, E. Gucciardi, A. Herrán, D. Carriazo, A. Villaverde, T. Rojo, *Molecules* **2020**, *25*, 2494.
[37] C. Heubner, T. Liebmann, O. Lohrberg, S. Cangaz, S. Maletti, A. Michaelis, *Batter. Supercaps.* **2022**, *5*, e202100182.
[38] K. Sato, A. Tamai, K. Ohara, H. Kiuchi, E. Matsubara, *J. Power Sources* **2022**, *535*, 231399.
[39] K. Richter, T. Waldmann, N. Paul, N. Jobst, R. G. Scurtu, M. Hofmann, R. Gilles, M. Wohlfahrt-Mehrens, *ChemSusChem* **2020**, *13*, 529.
[40] S. Dhillon, G. Hernández, N. P. Wagner, A. M. Svensson, D. Brandell, *Electrochim. Acta.* **2021**, *377*, 138067.
[41] J. Tao, L. Liu, J. Han, J. Peng, Y. Chen, Y. Yang, H. rong Yao, J. Li, Z. Huang, Y. Lin, *Energy Storage Mater.* **2023**, *60*, 102809.
[42] P. Limthongkul, Y. Il Jang, N. J. Dudney, Y. M. Chiang, *Acta Mater.* **2003**, *51*, 1103.
[43] M. N. Obrovac, L. J. Krause, *J. Electrochem. Soc.* **2007**, *154*, A103.
[44] C. L. Berhaut, M. Mirolo, D. Z. Dominguez, I. Martens, S. Pouget, N. Herlin-Boime, M. Chandesris, S. Tardif, J. Drnec, S. Lyonnard, *Adv. Energy Mater.* **2023**, *13*, 2301874.
[45] M. Zeilinger, V. Baran, L. van Wüllen, U. Häussermann, T. F. Fässler, *Chem. Mater.* **2013**, *25*, 4113.
[46] J. Li, J. R. Dahn, *J. Electrochem. Soc.* **2007**, *154*, A156.